

Accelerating and spatially-varying crustal uplift and its geomorphic expression, San Andreas Fault zone north of San Francisco, California

Karen Grove ^{a,*}, Leonard S. Sklar ^a, Anne Marie Scherer ^a, Gina Lee ^a, Jerry Davis ^b

^a Department of Geosciences, San Francisco State University, San Francisco, CA 94132, USA

^b Department of Geography and Human Environmental Studies, San Francisco State University, San Francisco, CA 94132, USA

ARTICLE INFO

Article history:

Received 1 April 2010

Received in revised form 16 September 2010

Accepted 22 September 2010

Available online 29 September 2010

Keywords:

Marine terrace

Luminescence dating

Hillslope gradient

Watershed hypsometry

Point Reyes

Marin County

ABSTRACT

Marine terraces that bevel the western flank of the Point Reyes Peninsula were used to measure crustal uplift rates west of the San Andreas Fault segment north of San Francisco. Field measurements of platform inner edges, and luminescence ages from overlying marine sediments, suggest the youngest platform was cut by waves during the ~80-ka sea-level high stand (MIS 5a). Since 80 ka, the platform has been uplifted slowly throughout most of the peninsula, but more rapidly in the southern part, where uplift reaches a rate of ~1 m/ka. Analyses of the spatial distributions of hillslope gradient and elevation are consistent with the terrace data. Correlations of older terrace levels to high-stand ages suggest that crustal uplift has accelerated in the southern part of the peninsula during the past ~300 ky, probably as a result of a contractional zone that has been migrating northward. This study is the first to quantify the rate and style of crustal uplift west of this San Andreas Fault segment. Although the transform motions in this region are well documented, the complex nature of interacting fault strands are only beginning to be understood. These results imply that other faults, with reverse-motions, are also active and potentially contributing to earthquake hazards.

© 2010 Elsevier B.V. All rights reserved.

1. Introduction

The San Andreas Fault (SAF) system in the San Francisco Bay Area is a complex strike–slip system (Fig. 1) with faults displaying vertical as well as horizontal motions. The horizontal component comprises motion on a series of sub-parallel faults with motion totaling 38–39 m/ka (Wakabayashi, 1999; Argus and Gordon, 2001; d'Alessio et al., 2005). A vertical component yields crustal uplift rates up to 1 m/ka; the compressional stress producing this uplift is a result of both local geometric effects (e.g., Santa Cruz Mountains—Anderson and Menking, 1994) and a change in plate vector at ~6.6 Ma that has produced a small component of fault-normal contraction and formed the California Coast Ranges (Argus and Gordon, 2001). Many investigations have focused on the SAF system, from where it splits from a single strand in central California into multiple strands around San Francisco Bay, but fewer have focused on the SAF's continuation north of San Francisco, where it separates mainland California from the Point Reyes Peninsula (PRP; Figs. 1 and 2) and where the offshore location of some faults has hampered their interpretation.

The PRP provides important on-land exposures of geologic features that extend into the offshore zone. McCulloch (1989) showed that the PRP is part of the eastern margin of the offshore Bodega Basin, where a thick sequence of mostly marine Cenozoic sedimentary rocks overlie

granitic and metamorphic basement of the Salinian terrane. As the site of a long-lived fold-and-thrust belt, these rocks have been deformed by numerous Cenozoic tectonic events, most recently since the Neogene initiation of the SAF transform system. Because offshore structures have deformed the Mio-Pliocene Purisima Formation, they have been assigned an early Pleistocene age (Hoskins and Griffiths, 1971), although how long they have continued to be active has remained uncertain. Initial studies of offshore seismic data, collected by petroleum companies and recently released to the public through the U.S. Geological Survey (<http://walrus.wr.usgs.gov/NAMSS/>), show that the offshore Point Reyes thrust may connect to the south with the western strand of the active San Gregorio Fault (Fig. 1; Grove and Ryan, 2007; Ryan et al., 2008). Farther south, more abundant active seismicity and numerous geophysical surveys have helped to interpret the geometry and activity of offshore faults west of the Golden Gate entrance to San Francisco Bay (e.g., Zoback et al., 1999; Bruns et al., 2002; Jachens et al., 2002). Recently collected high-resolution seismic data from this area (Bruns et al., 2002; Ryan et al., 2008) illustrate the complex interactions of offshore faults that connect between onshore positions on the San Francisco Peninsula (south of the Golden Gate) and Marin County (north of the Golden Gate; Fig. 1). Seismic data show multiple fault strands that either curve to the west around the PRP or coalesce south of the peninsula (Bruns et al., 2002). To the north, the SAF forms an exceptionally linear valley that extends from Bolinas Lagoon northward through Tomales Bay (Fig. 2).

The Point Reyes region is best known as the segment of the SAF where the largest amount of dextral displacement (more than 5 m) was

* Corresponding author. Tel.: +1 415 338 2617; fax: +1 415 338 7705.
E-mail address: kgrove@sfsu.edu (K. Grove).

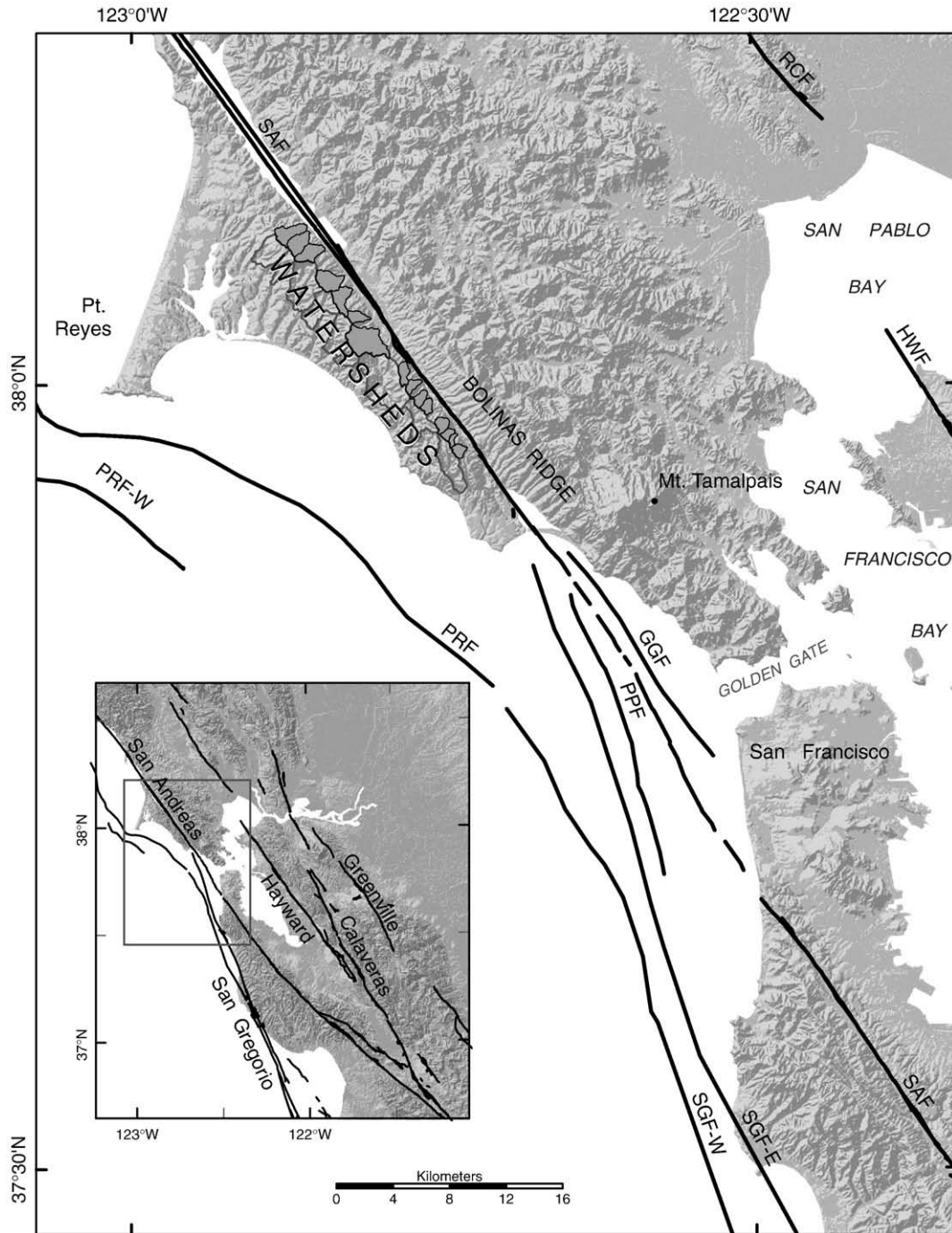


Fig. 1. Map of the San Francisco Bay Area, showing primary faults of the San Andreas Fault (SAF) system and watersheds used in geomorphic analysis. PRF=Point Reyes Fault (PRF-W=western strand); SGF-E/SGF-W=eastern and western strands of the San Gregorio Fault; PPF=Potato Patch Fault; GGF=Golden Gate Fault; HWF=Hayward Fault; RCF=Rogers Creek Fault. Quaternary faults from [<http://www.consrv.ca.gov/CGS>] and Ryan et al. (2008).

measured after the great 1906 San Francisco earthquake (Lawson, 1908). The measured Holocene dextral slip rate of 24 ± 3 m/ka for the Point Reyes segment of the SAF (Niemi and Hall, 1992) is higher than the measured 17 ± 4 m/ka slip rate on the San Francisco Peninsula segment (Hall et al., 1999) because it includes motion on the San Gregorio Fault (SGF) that joins the SAF near Bolinas (Fig. 1). Calculated slip rates based on offsets of older features suggest that the 24 ± 3 m/ka rate has been constant over the past 30 ky and perhaps longer (Grove and Niemi, 2005).

Whereas the strike-slip component of faulting on the Point Reyes segment of the fault has been extensively quantified, the dip-slip component has remained poorly understood. Since 1906, the SAF has been quiescent, and the entire Point Reyes region has experienced

little seismicity. The only earthquake with a >3 magnitude since 1906 was a $\sim M5$ event in 1999 with an epicenter at the western edge of the SAF zone near Bolinas (Fig. 2; NCEDC, 2004). The fault plane solution shows predominantly reverse motion on a northwest-trending fault (SEP, 1999). Given its proximity to the vertical SAF, the fault that produced this earthquake is probably east-dipping, perhaps connecting to the SAF at depth. Based on the 7 km hypocentral depth and the $\sim 45^\circ$ fault dip, the fault would project to the seafloor about 7 km west of the epicenter, near where the Point Reyes thrust has been mapped on the seafloor (Fig. 2). The 1999 Bolinas earthquake was the first direct evidence for vertical motion on faults that are accommodating the contractional component of strain in the region.

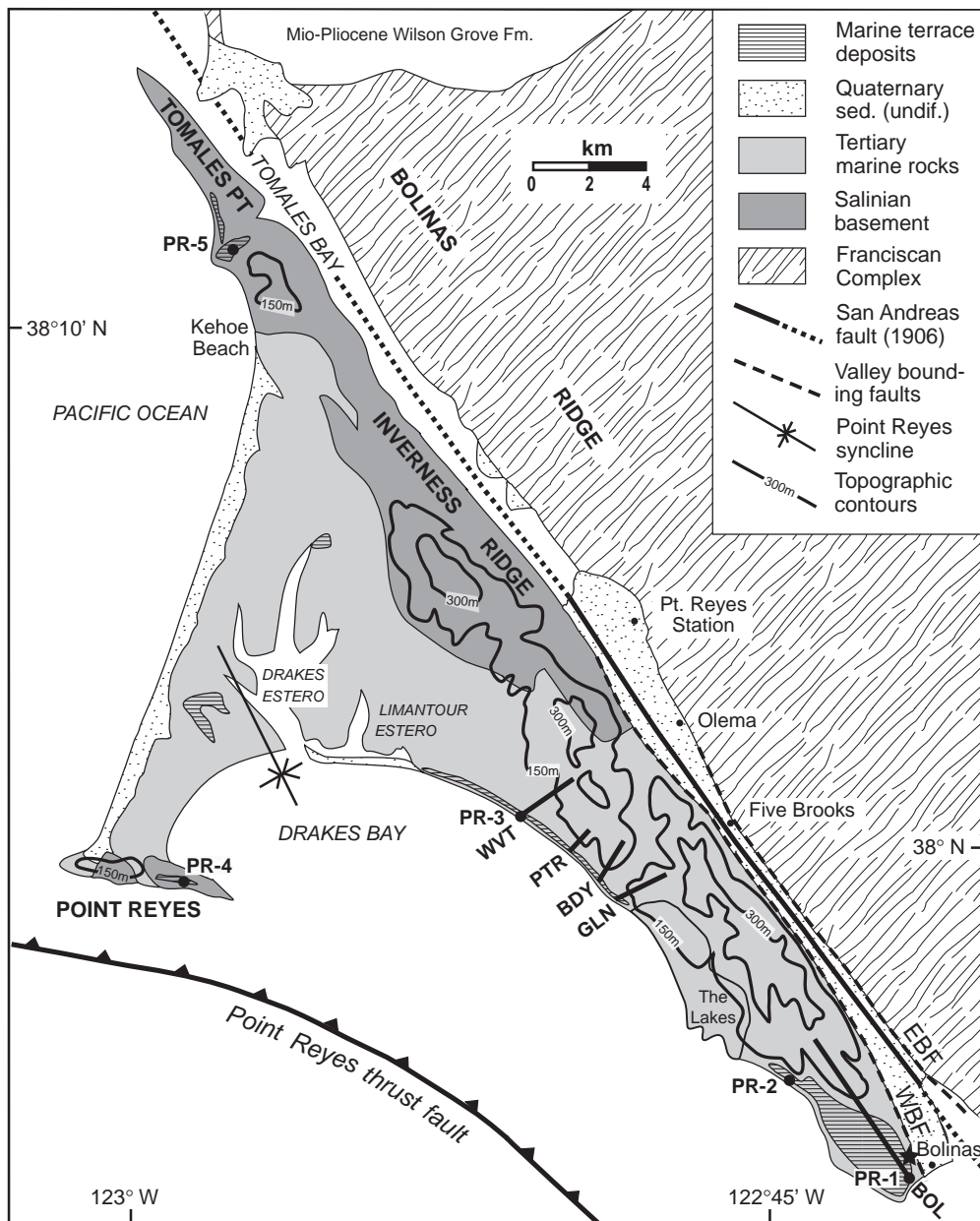


Fig. 2. Map of Point Reyes Peninsula; geology adapted from Clark and Brabb (1997); Point Reyes thrust location from Ryan et al. (2008). PR-1–5: sample sites for luminescence dating. Measured terrace flights: WVT (Woodward Valley transect); PTR (Point Resistance transect); BDY (Baldy transect); GLN (Glen transect); BOL (Bolinas transect). EBF = Eastern Boundary Fault; WBF = Western Boundary Fault (from Galloway, 1977). Black star at Bolinas = epicenter of ~5 M earthquake in 1999.

Marine and fluvial terraces that bevel the flanks of the ridges east and west of the SAF zone (Bolinas and Inverness Ridges, respectively) provide additional evidence for reverse fault motion at Point Reyes, where the ridges have been uplifted relative to the intervening fault valley (Fig. 2). We studied the marine terraces on the western flank of Inverness Ridge to gauge vertical strain, to estimate the rate and style of uplift of the peninsula, to assess the potential for reverse-motion earthquakes on local (probably offshore) faults, and to provide insight into the regional tectonic picture. After finding that uplift rates vary in both space and time, we analyzed geomorphic attributes to look for landscape signatures of the varying uplift rates.

In this paper, we present evidence for variable uplift throughout the peninsula and accelerating uplift during the past several hundred thousand years at the southern end. These results provide the first clear evidence for late Pleistocene uplift in the region and imply that some of the offshore thrust faults have continued to be active or have been rejuvenated. We also present results from our analysis of two

geomorphic attributes—we found that hypsometric and slope angle data are consistent with calculated differential uplift rates. An improved understanding of the abrupt spatial and temporal changes associated with faults of the SAF zone can help us to better evaluate the evolution of these types of major strike-slip systems and their potential earthquake hazards.

2. Regional geology

The PRP is bounded on the east by the SAF and on the west by the Pacific Ocean (Fig. 2). The peninsula is part of the Salinian terrane, a continental fragment that has been transported approximately 450 km northwest of its original location by right-lateral slip along the San Andreas and San Gregorio faults (Clark et al., 1984). As a result of this long-term dextral translation, the SAF zone, located within a linear valley between Bolinas Lagoon and Tomales Bay, juxtaposes Cretaceous magmatic arc rocks of the Salinian terrane to the west with

Upper Jurassic to Cretaceous subduction-complex rocks of the Franciscan Complex to the east (Fig. 2).

The SAF fault zone extends south of Bolinas into the tectonically-complex offshore region west of San Francisco. Analyses of high-resolution seismic reflection data by Bruns et al. (2002) have shown that the 1906 strand of the SAF lies in the middle of a Holocene basin bounded on the east by the Golden Gate Fault and on the west by the Potato Patch Fault, which extends between the San Gregorio Fault (SGF) to the south and the SAF to the north (Fig. 1). The 1906 SAF strand appears to be quite youthful, without large stratigraphic offset across it, and dextral slip has been transferred among a variety of faults in both time and space (Bruns et al., 2002). The Golden Gate Fault connects with the onshore Eastern Boundary Fault (EBF on Fig. 2), and south of Bolinas the Potato Patch Fault merges with the active SAF (Fig. 1). The eastern strand of the SGF, located ~1 km west of the SAF, appears to connect with the onshore Western Boundary Fault (WBF on Fig. 2). Although the seafloor has been extending between the San Andreas/Potato Patch Fault and the Golden Gate Fault, the seafloor is contracting a short distance to the west, where multiple fault strands (San Gregorio structural zone of Bruns et al., 2002) show evidence of recent folding and uplift extending northward onto the southern end of the PRP. The western strand of the SGF may connect to the northwest with the Point Reyes thrust fault (Ryan et al., 2008; Fig. 1). These faults may be responsible for the uplifted marine terraces observed on the PRP, a hypothesis we discuss below. This is also the region where the ~M5 reverse-motion earthquake occurred in 1999 (NCEDC, 2004).

The PRP consists of Salinian plutonic and older metamorphic basement rock overlain by over 4 km of Paleocene to Pliocene marine sedimentary rock that consists of conglomerate, sandstone, siltstone, and siliceous mudstone and chert, and Quaternary stream, beach, landslide and dune deposits (Galloway, 1977; Clark et al., 1984; Clark and Brabb, 1997). The geologic units have been folded into a broad syncline flanked by two anticlines that have been truncated by motions on the offshore Point Reyes thrust fault to the west (McCulloch, 1989) and possibly by the WBF to the east (Fig. 2). The synclinal fold is visible in the topography as the northwest–southeast-trending Inverness Ridge (eastern limb), the east–west-trending Point Reyes headland (western limb), and the low-lying Drakes Estero between the ridges (hinge area). Much of the marine sedimentary section has been removed on the uplifted ridges where basement is exposed, but complete sections have been described from bore holes in the syncline's center (Galloway, 1977) and from the offshore part of the basin (Hoskins and Griffiths, 1971; McCulloch, 1989). Uplifted coastal marine terraces that are best preserved on the eastern limb (Inverness Ridge) of the fold (Fig. 2) imply that thrust faults, mostly located in the offshore zone, continue to be active. We studied the marine terraces to better understand the rate and style of uplift and the role of contractional structures in this region that is best known for its transform structures.

3. Coastal uplift rates

Because uplifted marine terraces are best preserved on the eastern limb of the Point Reyes syncline, we focused our studies on terraces beveling the western flank of Inverness Ridge (Fig. 2). Marine terraces form along emergent coastlines by interaction between glacioeustatically controlled sea-level fluctuations and tectonic uplift. They consist of a bedrock platform that is sculpted by wave action during times of stable relative sea level and overlain by surficial sediments. Platforms are cut when the rate of sea-level rise exceeds or equals the rate of uplift during interstadial or interglacial sea-level rises and resultant sea-level high stands (Muhs, 2000). When the planet enters a glacial period, sea-level falls; meanwhile, regional uplift continues and the platform becomes abandoned. When sea level rises again during the next interglacial period, the process of shaping a wave-cut

platform begins again and a new platform is formed below the uplifted and abandoned platforms. As this cycle continued during the Pleistocene Epoch, sequences or “flights” of terraces formed along emergent coastlines around the world, such as in New Zealand (Claessens et al., 2009), southern Italy (Santoro et al., 2009), and Patagonia (Rostami et al., 2000). Terrace flights found along the Pacific coast have been used extensively to understand the uplift history of the region (e.g., Merritts and Bull, 1989; McInelly and Kelsey, 1990; Anderson and Menking, 1994; Muhs et al., 2003a), but they have not been previously studied at Point Reyes.

Because marine terraces are formed at a known datum (sea level), flights of uplifted terraces can be used as strain gauges if the amount of uplift can be measured and the terrace platforms can be dated (Lajoie, 1986). The marine terraces now exposed on-land were formed at sea-level high stands and they can be correlated to the marine oxygen isotope (MIS) record, which is a function of ocean temperature and ice volume and serves as a proxy for global sea level (Lisiecki and Raymo, 2005). Uranium-series dating of carbonate from tropical coral reefs (e.g., Huon Peninsula, New Guinea; Chappell and Shackleton, 1986; Chappell et al., 1996) and from solitary corals in terrace sediments (e.g., Pacific Coast of North America; Muhs et al., 1994) has been used to provide elevations of paleo-sea-level high stands and to correlate terrace flights with the MIS record. At Point Reyes we measured the elevations of wave-cut platforms and estimated the ages of the surfaces, as described below. Uplift rates were then calculated by dividing the amount of vertical displacement by the age after correction for paleo-sea level.

3.1. Terrace elevation measurements

To calculate the amount of coastal uplift, we used a differential carrier-phase GPS unit (Trimble Pro XRS) to measure the horizontal locations and elevations of marine terraces along coast-normal transects on the interflues where morphological surfaces are preserved between erosional valleys (Fig. 2). An average of 24 logged positions at each point was recorded to achieve sub-meter elevation accuracy, based on our experiments at benchmarks of known elevation. A coastal geodetic station was used to make real-time corrections to GPS measurements in the field and maximize instrumental precision. Terrace surfaces were correlated across the erosional valleys between transects using map relationships and visual evaluations aided by a hand level.

The GPS unit was used to measure xyz positions of inner-edge, riser, outer-edge, and mid-terrace points on the terraced landforms (Figs. 3 and 4; Table 1). The most important feature is the platform inner edge, which is the line of intersection between the bedrock platform and the ancient sea cliff. Because the inner edge forms at sea level, it is the best approximation of the shoreline position at the time the platform was created. On terrace level 1, the youngest, lowest-elevation terrace, the inner edge is buried beneath a sediment sequence that decreases from ~34-m-thick at WVT to ~4-m-thick at BOL (Table 1). To estimate the inner-edge elevations, we measured positions in the valleys between interflues, where buried platforms

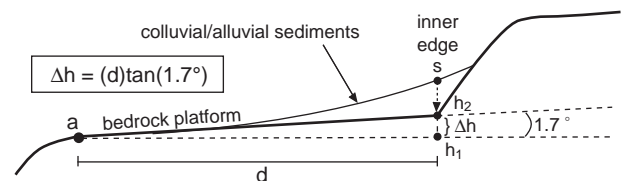


Fig. 3. Technique used to estimate elevation of terrace inner-edge (h_2), where buried beneath sediment cover and not visible in valleys between interflues. Measured elevation of terrace outer edge (position “a”, at elevation h_1) is projected to inner-edge position estimated from inflection on surface of overlying colluvial/alluvial wedge (position “s”); d = horizontal distance between outer and inner-edge positions. Δh = estimated elevation difference between measured outer-edge and inner-edge elevations calculated using bedrock platform slope of 1.7° (see text for explanation).

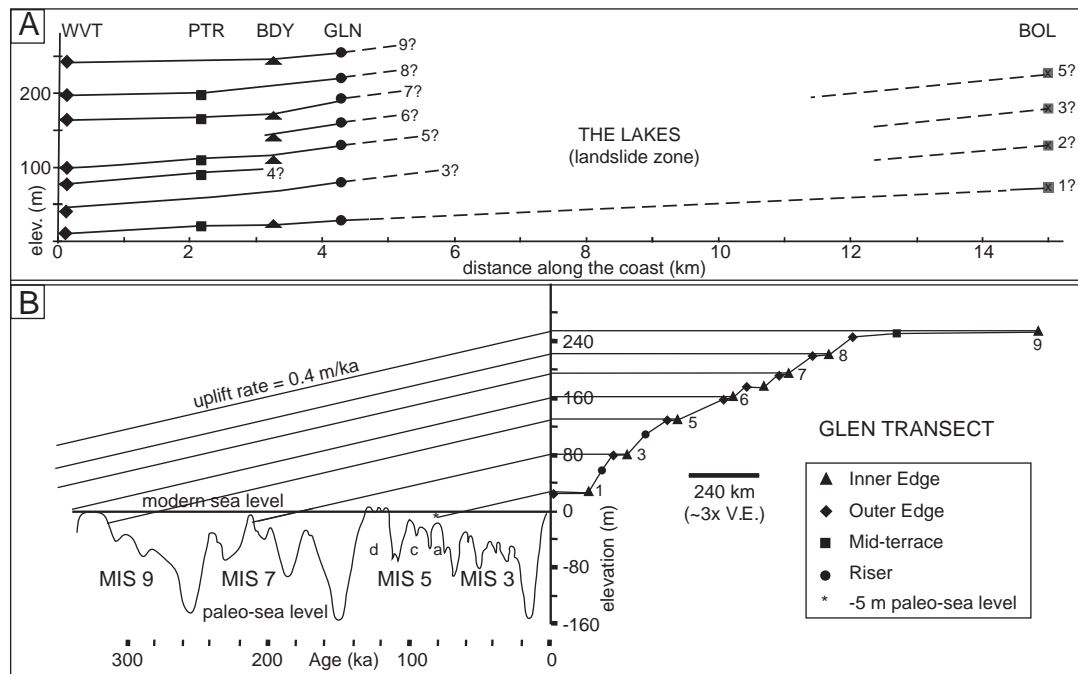


Fig. 4. A) Inner-edge elevations of terraces as a function of distance along the coast, measured from the WVT transect (see Fig. 2 for transect locations and abbreviations). Queried numbers are terrace levels, as in Fig. 5. Inner edges along each transect were projected onto a trend line oriented perpendicular to the coast, with projection amounts not exceeding 200 m. Note that trend lines are oriented NE–SW for WVT–GLN transects and NW–SE for BOL transect. B) Example terrace flight (GLN transect) and correlation between platform elevations and sea-level high stands extending back to MIS (marine isotope stage) 9, assuming constant crustal uplift rate of 0.4 m/ka. Paleo-sea level (–5 m) of MIS 5a from Muhs et al. (1994).

Table 1
Terrace data and calculated uplift rates from field measurements on western flank of Inverness Ridge.

Transect	Terrace width (m) ^a	Inner-edge elev. (m) ^b	Outer-edge elev., h_1 (m) ^c	Elev. change, Δh (m)	Corrected inner-edge elev., h_2 (m)	Sed. thickness (m)	Amount of uplift (m) ^d	Estimated age (ka) ^e	Uplift rate (m/ka) ^f	Terrace level ^g
WVT	170	45	6	5.2	11	33	16 ^d	80	0.20	1
	122	46	35	4.4	39	7	44	200	0.22	3
	31	77	70		77		77	240	0.32	4
	21	99	91		99		99	330	0.30	5
	364	164	161		164		164	490	0.33	7
PTR	172	197	185		197		197	570	0.34	8
	282	242	245		242		242	700	0.34	9
	303	46	13	9.0	22		27 ^d	80	0.34	1
	38	97	89	1.1	90		90	240	0.37	4
	11	110	108	0.3	108		108	330	0.33	5
BDY	87	168	161	2.6	164		164	490	0.33	7
	19	204	196	0.6	197		197	570	0.34	8
	104	40	18	3.1	21	24	26 ^d	80	0.32	1
	88	106	101		106		106	330	0.32	5
	10	138	136		138		138	410	0.34	6
GLN	47	169	164		169		169	490	0.34	7
	267	241	236		241		241	700	0.34	9
	124	38	24	3.7	28	10	33 ^d	80	0.40	1
	51	91	78	1.5	80		80	200	0.40	3
	39	129	128		129		129	330	0.39	5
BOL	33	161	157		161		161	410	0.39	6
	36	194	190		194		194	490	0.39	7
	62	221	218		221		221	570	0.39	8
	685	255	245		255		255	700	0.36	9
	1735	77	43		77	4	82 ^d	80	1.03	1
BOL	60	142	140		142		136	125	1.08	2
	215	179	158		179		179	200	0.90	3
	744	228	220		228		228	330	0.69	5

^a Horizontal distance between terrace inner edge and outer edge.

^b GPS elevation above inner edge (position “s” on Fig. 3) if correction (Δh) applied; on bedrock if no correction (Δh) applied.

^c GPS elevation on bedrock at terrace outer edge.

^d Paleo-sea level correction of +5 m applied to 80-ka (MIS 5a) terrace level; no correction applied to higher levels.

^e Age of terrace level 1 based on luminescence data. Other ages based on correlations to sea-level high stands (Fig. 5).

^f Uncertainty of ± 0.04 m/ka for terrace level 1.

^g Terrace levels shown on Figs. 4 and 5.

were sometimes visible, and projected elevations from outer-edge positions (Fig. 3). The projection method uses data collected by Bradley and Griggs (1976), who created coastline-orthogonal profiles of wave-cut platforms that are well preserved in the Santa Cruz Mountains south of San Francisco. They used direct platform measurements and, where exposures were absent, located the platforms with a refraction seismograph. They found that older terraces had progressively greater seaward gradients, but that the youngest terraces had seaward gradients similar to those measured on the modern wave-cut platform with fathometer surveys (Bradley and Griggs, 1976). The gradients were consistently 0.02 to 0.04 on the inshore segments (inner 300–600 m), and 0.007–0.017 on the offshore segments. The youngest terrace level on the WVT to GLN transects is ≤ 300 m wide (Table 1), so we used the average of the inshore segment gradients ($0.03 = \tan 1.7^\circ$). At the WVT, PRT, and GLN transects, we were able to directly view terrace inner edges and refine the projection calculations. In contrast to the WVT–GLN transects, the youngest terrace level on the BOL transect is very wide (Table 1). Fortunately, we were able to measure this inner-edge position directly, where it is exposed in an eroded gully. Water-well logs near the inner-edge position showed a bedrock depth consistent with the direct inner-edge measurement. The gradient of this platform is somewhat smaller (~ 0.019) than those to the north, because it is >1700 -m wide and includes a more offshore, lower-gradient segment.

Elevations of older terrace inner edges are less certain because the sediment cover has been mostly eroded from higher terrace levels and the bedrock platforms themselves are commonly eroded. An exception is the WVT transect, where terrace level 3 is buried by the 34-m-thick sediment cover (Table 1). Both the outer and inner edges of this terrace were visible in the eroded valley adjacent to the transect and elevations could be measured with more certainty. On some terrace levels, corrections were applied where the platform is covered by vegetation and soil (all levels on PTR transect and level 3 on GLN transect; Table 1). The preserved platforms are very narrow (<80 m wide) and the correction has an uncertainty of ± 1 m. Most of the higher terraces have exposed platform surfaces and it was possible to measure the inner-edge elevation directly. These elevations are minimum values because the amount of erosion is uncertain. For example, terrace level 9 on the WVT transect has an inner-edge elevation that is lower than the outer-edge elevation. We estimate an uncertainty of ± 5 m for the higher terrace levels. Corrected inner-edge elevations for all terrace levels along the coast are depicted in Fig. 4A.

Although wave-cut platforms are created during stable sea-level low stands as well as high stands, the low-stand platforms are now submerged, and we can assume that the exposed platforms were created during high stands. Because past high stands reached different elevations than today's high stand, we used estimates of past sea-level elevations (Chappell and Shackleton, 1986; Muhs et al., 1994; Chappell et al., 1996) to determine the amount of uplift (terrace level 1 on Table 1). To calculate the total vertical displacement of a marine platform, the elevation of the past eustatic sea level must be subtracted from the present elevation of the terrace if the past level was higher than today and added from the present elevation if the past level was lower than today. The record of paleo-sea levels is complicated by differential glacio-hydro-isostatic responses of Earth's crust (Muhs et al., 2003b). For example, estimates for the MIS 5a level range from -25 m (Chappell and Shackleton, 1986) to -5 m (Muhs et al., 1994). We used a correction of $+5$ m for the youngest terrace (level 1) because studies along the Pacific Coast of the United States suggest that the 5a level at this location was close to the present-day level (Muhs et al., 1994, 2003b). Corrections were applied only to the youngest terraces; the correction is poorly known for high stands older than 125 ka and it would be too small to affect the uplift rate when averaged over longer time periods.

To plot profiles for each transect (e.g., GLN transect in Fig. 4B), we projected GPS position data onto best-fit lines oriented perpendicular

to the coast. We also used ArcGIS 8.3 (Environmental Systems Research Institute, 1999–2009) to compile, analyze and display collected elevation data. The layers included imported digital elevation models (DEM), digital orthophoto quarter-quads (DOQQ), and a geologic map (Clark and Brabb, 1997); field-measured GPS terrace data; hillshade, contour, slope and aspect layers created using the Spatial Analyst extension. The GIS map was used to further interpolate between measured inner-edge points, to delineate locations of 9 paleo-shorelines, and to outline remnant terrace landforms for the 9 terrace levels (Scherer, 2004).

In summary, terrace elevation data for the lowest (i.e., youngest) platform are most certain. The lowest level is exposed along the coast, where the bedrock platform and overlying sediments are clearly visible. The lowest terrace level is deformed; although created as a horizontal surface, the platform's inner-edge elevation now increases south along the coast, changing from ~ 11 m at the Woodward Valley (WVT) transect to ~ 77 m at the Bolinas transect (Table 1; Fig. 4A). Higher (i.e., older) terraces are more discontinuous than the lower ones because of erosion that has dissected surfaces and removed surface sediments. Terraces at all levels are discontinuous in an extensive landslide zone between the GLN and BOL transects (The Lakes region on Fig. 2) that has disrupted the surfaces and formed slump blocks where water has accumulated as lakes. Clague (1969) determined that the landslide zone has continued to be active, most recently during the great San Francisco earthquake of 1906.

3.2. Terrace age data

To determine the age of a wave-cut platform, it is necessary to date the surficial sediments deposited on top of the platform. If the sediment is marine sand, it was probably deposited on the platform during the high stand associated with platform creation; if the sediment is alluvium or colluvium, it was probably deposited after that high stand. The best technique for obtaining numerical ages of marine terraces, most of which are older than the practical limits of radiocarbon dating, is U-series dating of fossils that are found in marine deposits and assumed to be the same age as the platform. Corals, including solitary forms found in California and Oregon, are most commonly used because they demonstrate closed-system conditions and continue to take up U from sea water during their growth (Muhs et al., 2002).

Where fossils are not present, other techniques are used that date individual sediment grains assumed to have been buried shortly after the marine platform was created. Cosmogenic dating techniques use inventories of ^{10}Be and ^{26}Al that act as clocks reset by cosmogenic rays before burial; terrace ages have been estimated where complete sediment sequences can be used to measure a decay profile (Perg et al., 2001). Luminescence dating techniques are based on the ability of quartz and feldspar minerals to trap electrons in structural defects of their crystalline structure when exposed to ionizing radiation (e.g., alpha, beta, and gamma), thus storing an increasing amount of energy over time (Duller, 2004). Sediments are “reset” (i.e., traps are emptied), and the stored energy is released, when crystals are exposed to light during erosion; if subsequently buried, the sediment grains will trap irradiation energy anew. In the lab, the trapped energy can be released by stimulating samples with heat (thermoluminescence—TL) or light (optically-stimulated luminescence—OSL), and the resultant light energy can be measured (a quantity called the equivalent dose—De) (Duller, 2004). Ages are determined by dividing the equivalent dose (SI units of grays—Gy) by the dose rate—D (Gy kyr^{-1} ; determined by experiment; Duller, 2004). The current upper limit of the technique is several hundreds of thousands of years (although theoretically it could be extended to >1 Ma), determined by the amount of time it takes for all of the sediment traps to be filled in, when no more energy can be stored—a condition called “saturation” (Lian and Roberts, 2006; Prescott and Robertson, 2008). The technique can be used to date very young sediments, but too-young ages

can be obtained if, after burial, sediments are eroded, reset, and reburied (Burbank and Anderson, 2001), or if the luminescence signal in feldspar grains fades over time (Prescott and Robertson, 2008). Too-old ages can be obtained if sediments did not receive sufficient sunlight to completely reset the signal prior to burial (Lian and Roberts, 2006).

At Point Reyes, we used marine sediments on the lowest terrace platform for luminescence dating because no fossils have been found (Table 2). On the lowest platform surface along Inverness Ridge, complete sequences with marine sand at the base are preserved at the south end of the peninsula near Bolinas, our best sites for luminescence dating (PR-1 and PR-2; sampling locations shown on Fig. 2). Farther north, most of the marine sand has been eroded away and the platform is overlain by ~30 m of alluvial sediment. Here, small amounts of marine sand have been preserved but, because the sediment was exposed to erosion prior to deposition of the alluvium, the age from the Woodward Valley transect is a minimum age (PR-3 on Tables 2 and 3). Older (i.e., higher elevation) terraces are almost completely stripped of sediment, so we estimated their ages using graphical techniques (Lajoie, 1986; Muhs, 2000) that correlate terrace levels with global sea-level data based on the deep-sea record of marine oxygen isotope stages (MIS) and well-dated coral-reef strandlines on the Huon Peninsula (Chappell and Shackleton, 1986).

Samples were collected to avoid light contamination by removing surface sediments, pounding a 30-cm-long black PVC tube into the cliff face, extracting the tube under an opaque black cloth, and covering ends with duct tape. Samples were submitted to the U.S. Geological Survey (USGS) Luminescence Dating Laboratory in Denver, operated by S. Mahan, for analysis. Dose rates (D) were determined using gamma ray spectrometry and computed from concentrations of K, U, and Th (Table 2), following the method of Aitken (1998). Field moisture conditions were measured using separate bulk samples. Because the water content of a sediment affects the rate at which the sediment stores irradiation energy (more pore-space water acts to attenuate the signal) we were provided with ages based on three dose rate calculations: (1) age if moisture conditions were always as sampled in the field; (2) age if sample had always been completely saturated; (3) age if moisture conditions were half-way between field and saturated conditions. We choose the half-way calculation (Table 2) because the samples were collected in July, a dry time in California, after months of no rain, and with less saturated conditions then during the rainy winter season when terrace surfaces often flood and sediments reach complete saturation.

Equivalent dose (De) values were obtained using three types of energy stimuli—optically-stimulated blue-light luminescence (blue-OSL), optically-stimulated infra-red luminescence (IRSL), and thermoluminescence (TL) (Table 3). The USGS lab uses the “total bleach” method for TL and the “additive dose” method for optical luminescence. Tests for anomalous fading and signal stability (plateau test) were applied. A full explanation of USGS lab procedures is available in Millard and Maat (1994) and in an updated web site: http://crustal.usgs.gov/laboratories/luminescence_dating/.

Table 2
Samples collected for luminescence dating from marine terrace sediments, Point Reyes Peninsula.

Sample ID	Latitude (°N)	Longitude (°W)	Sample altitude (m)	Sample depth (m) ^d	Field H ₂ O content (%)	Saturated H ₂ O content (%)	Used H ₂ O content (%)	K (%)	Th (ppm)	U (ppm)
^a PR-1	37.9000	122.6938	49.8	4	6	40	23	0.96	0.84	2.35
^a PR-2	37.9223	122.7333	64.3	9	6	28	17	0.67	1.19	2.77
^a PR-3	38.0134	122.8505	5.6	39	10	45	27.5	1.22	1.62	3.90
^b PR-4	37.9937	122.9827	103.2	3	5.5	40	22.5	3.22	5.80	4.03
^c PR-5	38.1868	122.9571	85.6	15	4	30	17	0.70	0.94	2.56

^a Beach sediments overlying youngest wave-cut platform.

^b Sediments of uncertain origin overlying bedrock on Point Reyes headland.

^c Eolian sediments on hillslope.

^d Depth below terrace surface.

Table 3
Luminescence age data from Point Reyes Peninsula.

Sample ID/method	n ^d	De (Gy/ka)	D (Gy)	Age (ka)	Interpretation—MIS stage
PR-1/OSL ^a	28	32.26 ± 1.32	1.06 ± 1.3	30.43 ± 1.13	MIS 4 (~65 ka)
PR-1/IRSL ^b	28	102.93 ± 0.81	1.56 ± 1.2	65.98 ± 1.91	
PR-1/TL ^c	15	128.47 ± 0.87	1.56 ± 1.2	82.35 ± 2.44	
PR-2/OSL ^a	13	53.29 ± 2.26	1.04 ± 2.4	51.24 ± 3.38	MIS 5a (~80 ka)
PR-2/IRSL ^b	24	132.62 ± 1.58	1.54 ± 1.1	86.12 ± 3.31	
PR-2/TL ^c	11	181.90 ± 2.07	1.54 ± 1.1	118.11 ± 5.55	
PR-3/OSL ^a	21	40.49 ± 0.97	1.41 ± 1.5	28.72 ± 1.03	MIS 3 (~45 ka) ^e
PR-3/IRSL ^b	29	85.56 ± 0.72	2.09 ± 1.4	40.98 ± 1.29	
PR-3/TL ^c	26	97.23 ± 1.63	2.09 ± 1.4	46.56 ± 2.00	
PR-4/OSL ^a	20	86.65 ± 0.17	3.95 ± 0.9	21.94 ± 0.40	Uncertain
PR-4/IRSL ^b	29	423.12 ± 0.74	5.85 ± 0.9	72.33 ± 1.69	
PR-4/TL ^c	7	583.17 ± 2.33	5.85 ± 0.9	99.69 ± 4.97	
PR-5/OSL ^a	12	82.47 ± 3.65	0.95 ± 1.3	86.82 ± 6.73	MIS 5a (~80 ka)
PR-5/IRSL ^b	29	96.21 ± 0.66	1.41 ± 1.2	68.47 ± 1.88	
PR-5/TL ^c	10	107.79 ± 1.08	1.41 ± 1.2	76.72 ± 2.48	

^a OSL on 90–125 μm quartz grains using single aliquot analyses.

^b IRSL on 4–11 μm feldspar grains using multi-aliquot analyses.

^c TL on 4–11 μm quartz and feldspar grains using multi-aliquot analyses.

^d Number of replicated equivalent dose (De) estimates used to calculate the mean.

^e Sediments deposited during OIS 5a but reset during post-OIS 5a erosion—see text.

Although results are inconsistent, we interpret the age of the lowest platform as ~80 ka, the last time sea level was nearly as high as it is today, during MIS 5a. This age corresponds to the ages obtained from the lowest terrace at the two closest locations dated by the U-series method on corals—Point Arena to the north (Muhs et al., 1990, 1994) and Point Año Nuevo to the south (Muhs et al., 2003a; but note that other methods have yielded ages ranging between the MIS 3 and MIS 5e high stands—e.g., Perg et al., 2001; Bradley and Griggs, 1976). Most of the inconsistency between sampled sites can be explained by their different stratigraphic positions and erosional history.

Inconsistencies within sites are at least partially the result of differences between the three luminescence techniques. In any crystal there are many kinds of electron traps; some traps are emptied easily when stimulated by light (blue-OSL), whereas others can be emptied only by heat stimulation (TL) (Lian and Roberts, 2006). According to S. Mahan (2002, pers. comm.), the OSL technique in her laboratory consistently yields ages that are probably too young. The OSL (blue-light) signal is most easily reset to zero and these traps become saturated more quickly (Duller, 2004); in this study we have largely discounted the OSL results as being improbably too young. According to S. Mahan (2002), the TL technique provides the maximum possible age; this signal does not saturate easily and is less easily reset. Some of the ages in our study may be too old because of a few older un-reset grains in the mix. The IRSL ages fall in between the blue-OSL and the TL ages and may be the best estimates of the depositional ages.

Results from site PR-2 (Fig. 2, Table 3) are the best indicator of the age of the youngest wave-cut platform. The site is only ~450 m from the platform inner edge, and the sample was collected from marine sand directly overlying the bedrock platform, at the base of a 9-m-thick

regressive sequence with no evidence of internal erosion between the marine and alluvial parts of the sequence. The sampled well-sorted, fine–medium sand is interpreted as beach sand, deposited in the foreshore–backshore zone where wave swash and wind are the dominant processes. Previous luminescence studies using beach sand from modern beaches and MIS-5-aged terraces suggest that beach sediments can receive sufficient light to be well bleached prior to burial (e.g., Richardson, 2001; Murray and Funder, 2003; Litchfield and Lian, 2004). Nevertheless, sample PR-2, although well behaved and exhibiting a good plateau, appeared to contain a mixed population including younger reset grains and older, non-zeroed grains, which may account for the older TL age (S. Mahan, 2002, pers. comm.). The beach sand was certainly deposited during a sea-level high stand, and the most likely one appears to be the MIS 5a high stand (age of IRSL result), because the ages are too young to correspond to the MIS 5c (~105 ka) high stand, and too old for the MIS 3 (~55 ka) high stand.

There is more consistency between the IRSL and TL results of sample PR-1 (Table 3), which was also collected from the base of a regressive sequence (4-m-thick) with no evidence of internal erosion. The site is located about 5 km from the inner-edge of the wave-cut platform (Fig. 2) and the beach sand was probably deposited after sea level had begun to fall from its high-stand position. The age of this sample is interpreted as late MIS 5a–early MIS 4.

Sample PR-3 was collected at the coastal end of the Woodward Valley transect (WVT; Fig. 2) from a thin beach sand that is separated from a thick overlying alluvial sequence by an erosional unconformity. Most of the beach sand was eroded away prior to deposition of the alluvium and the age therefore reflects the resetting of grains during this erosion event. The TL results yielded classic plateaus and ages similar to the IRSL results, indicating long exposures to the sun (S. Mahan, 2002, pers. comm.). Results are also similar to a 54.5 ± 3.7 ka radiocarbon (AMS) age (G. Seitz, 2002, pers. comm.) on a charcoal sample extracted from fine-grained sediment collected at the base of the alluvial sequence, although the age is near the limit of the method and may not be reliable. Sample RP-3 was collected close to modern sea level and it may have experienced more saturated conditions than the other samples; IRSL and TL ages for fully saturated conditions are ~48 ka and ~54 ka, respectively. The beach sand was probably deposited during the MIS 5a high stand, but then reset during a subsequence erosion event 45–55 ka (MIS 3). The age of the overlying alluvial sequence, which was deposited after the erosional event, is bracketed by the ages of the underlying beach sand and the ~10–7 ka radiocarbon ages obtained from pollen and wood charcoal collected in younger alluvial channels inset into the older alluvium (Rypins et al., 1989).

Sample PR-4 was collected from surficial sediment overlying a platform cut on granodioritic basement rock on the Point Reyes headland (west limb of large-scale fold; Fig. 2), where there is only one terrace level. Measured dose rates for this sample were much higher than for the other samples because of high quantities of K, U, and Th (Table 2). Ages are highly inconsistent (Table 3) and the depositional environment of the sediment unclear; the surface is unlikely to be younger than the MIS 5a high stand, but it could be somewhat older.

Sample PR-5 was collected from a ~20-m-thick sequence of beach/dune sand that fills a valley cut into basement rock on the northern end of the peninsula at Tomales Point (Fig. 2). The deposits have been uplifted, incised and inset by younger sand bodies in the lower parts of the valley. Results show the most internal consistency, indicating that everything in the sample was probably well mixed and bleached at about the same time, prior to burial. The sand was probably deposited during the latter part of MIS 5a (age range of 68–86 ka), as sea level was falling and exposing sand that was blown landward by wind. The initial elevation of these wind-blown deposits is uncertain so an uplift rate cannot be calculated.

In summary, age data are most consistent with formation of the youngest wave-cut platform along the west flank of Inverness Ridge

during MIS 5a. Future studies may resolve apparent inconsistencies in the dating results.

3.3. Calculated uplift rates—spatial variations

For the youngest terrace surface, we used our measured uplift amounts, after correction for paleo-sea level, and estimated 80-ka age to calculate uplift rates, which range from 0.2 ± 0.04 m/ka at the Woodward Valley transect to 1.0 ± 0.04 m/ka at the Bolinas transect (Table 1; Fig. 4A). Uncertainties are based on our estimate of ± 3.4 m total uncertainty in the elevation measurements resulting from instrumental error (± 1.0 m), irregularities inherent in the surface of wave-cut platforms (± 1.0 m, according to Bradley and Griggs, 1976), imprecision in locating the terrace inner-edge (± 0.4 m), and uncertainty in projecting elevation measurements from terrace outer to inner edges (± 1.0 m). As explained in Section 3.1, the uncertainty was reduced where the inner-edge position was viewed directly; this was particularly important for the transect at Bolinas, because the lowest terrace there is very wide (Fig. 2). A total uncertainty of ± 3.4 m yields an uncertainty in calculated uplift rates of the lowest terrace (formed ~80 ka) of ± 0.04 m/ka. Uplift rates on Table 1 are expressed to the nearest 0.01 m/ka, but may only be significant to the nearest 0.1 m/ka.

As described in Section 3.1, we added 5 m to the measured inner-edge elevations of terrace level 1 (Table 1), because paleo-sea levels along the Pacific coast of North America during the MIS 5a high stand (~80 ka) were apparently closer to modern sea level than at other locations (Chappell and Shackleton, 1986; Muhs et al., 1994). Similarly, paleo-sea levels during the MIS 5c high stand (~105 ka) are estimated at –7 m along the Pacific coast (Muhs et al., 1994) compared to –18 m in New Guinea (Chappell and Shackleton, 1986). In both locations, the paleo-sea level during the MIS 5e high stand (~125 ka) is estimated at +6 m. If luminescence ages are incorrect and the lowest terrace was actually created during the 5c high stand (adding 7 m to uplift amounts and dividing by 105 ky), uplift rates would change little, ranging from 0.2 m/ka at Woodward Valley to 0.8 m/ka at Bolinas. This level is rarely preserved along the California coast, where uplift rates are low to moderate and the 5a high stand appears to have reoccupied the platform created during the 5c high stand (Muhs et al., 1994). If the lowest terrace was created during the 5e high stand (subtracting 6 m from uplift amounts and dividing by 125 ky), uplift rates would be significantly lower, ranging from 0.0 m/ka to 0.6 m/ka; however, the luminescence results are far too young to support this interpretation. The MIS 3 high stand (~55 ka) was at a substantially lower level than today and would imply improbably high uplift rates near Bolinas (>2 m/ka). Whatever the age of the youngest platform, its increased elevation to the south indicates that the rate it is being uplifted is higher to the south.

The spatial variations in uplift along the coast of Inverness Ridge show that the Point Reyes Peninsula is not only translating northwestward because of dextral motions on faults of the SAF system, but that it is also being actively uplifted because of motion on reverse faults in the region. We interpret the southerly increase in uplift between the Woodward Valley and Bolinas transects to be a result of increasing proximity to the faults responsible for the uplift. The large-scale synclinal form of the peninsula is a result of fault proximity. The low-lying hinge region around Drakes Estero is farther from the active faults, whereas the topographically high ridges—the fold's eastern limb at Inverness Ridge and its western limb at the Point Reyes headland—are closer to the active faults. The eastern limb is truncated and bounded to the east by the linear edge of the SAF valley. Although not identified as active, based on its strong topographic expression, Galloway (1977) called this lineation the Western Boundary Fault (WBF), which may be partially responsible for uplifting the eastern limb. Offshore seismic data have revealed a series of reverse faults south of Bolinas between SGF-E and SGF-W/PRF (Fig. 1; Bruns et al.,

2002) that we hypothesize may be responsible for the increased rate of uplift at the south end of the peninsula (Grove and Ryan, 2007). It was probably motion on one of these faults, the westernmost of which appear to connect to faults of the PRF zone, that produced the ~M5 reverse-motion earthquake in 1999 (Fig. 2).

It is interesting to note that Kirby et al. (2007) also found increasing elevations to the south along Bolinas Ridge, which runs parallel to Inverness Ridge on the east side of the SAF. Their geomorphic analyses suggested that the increased elevation reflects an increase in crustal uplift to the south, a differential gradient that was attributed to a blind thrust fault beneath Mt. Tamalpais, located at the south end of Bolinas Ridge (Kirby et al., 2007). According to Johnson et al. (2009), the thrust could be functioning to make up a slip deficit between the SAF and Hayward/Rogers Creek faults. It seems unlikely that large shallowly-dipping structures like thrust faults could cross the ~vertical SAF, and structures that may be responsible for Inverness Ridge uplift can be identified on the seafloor south and west of the peninsula (Fig. 1). The southward increase in uplift rates on both sides of the fault is probably coincidental and, as described below, the elevation of Inverness Ridge does not increase dramatically to the south as it does along Bolinas Ridge.

3.4. Calculated uplift rates—temporal variations

Because sediments have been eroded from the older terrace surfaces, we used graphical methods to try to correlate inner-edge elevations of older marine platforms to previous sea-level high stands (Figs. 4 and 5; methodologies presented in Lajoie, 1986; Muhs, 2000). The most commonly used methods assume a constant uplift rate through time; however, using these methods for the terraces along Inverness Ridge produced different ages in the south for laterally continuous terraces. We also observed that if uplift rates near Bolinas had remained a constant 1.0 ± 0.04 m/ka for the past 800 ka, the southern part of the ridge would be more than 800 m above sea level, ignoring erosion. However, the highest part of Inverness Ridge is Mount Wittenberg, which is only 429 m above sea level, and the southern end of the ridge near Bolinas is even lower. We used a plot of inner-edge elevations as a function of uplift rate (Fig. 5) to explore various uplift scenarios. While not the only possible model, the one that seems to best fit all of our observations implies that uplift rates were lower in the past, particularly in the southern part of the ridge, where uplift appears to have been accelerating since at least 320 ka (Fig. 5). In contrast, uplift rates in the central part of the ridge appear to have remained steady for at least 700 ky. We emphasize that correlations with older sea-level high stands are highly tenuous and subject to revision with the addition of more age data. Other models

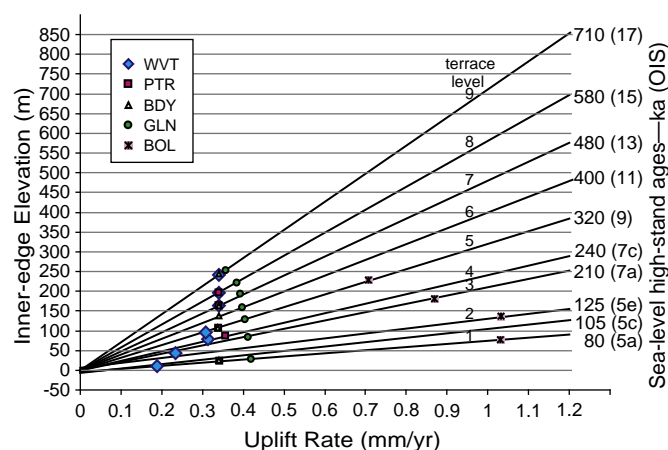


Fig. 5. Graph of varying uplift rates along the coast (see Fig. 2 for transect abbreviations). Sea-level high stand ages from Lisiecki and Raymo, 2005.

could be created from these data, but models must show a southward-increasing uplift rate for the youngest terrace and correlation among the older terraces that we have been able to visually correlate along the central part of Inverness Ridge. The large landslide zone (The Lakes on Fig. 2) has disrupted most terrace levels and it impedes our ability to connect central peninsula transects with the Bolinas transect farther south. Although we identified 11 terrace levels (Scherer, 2004), the upper two levels are highly-eroded ridge crests that lack identifiable platform inner edges.

Other observations are consistent with an accelerating uplift rate at the southern end of the PRP, near Bolinas. Recent seismic data collected in the offshore zone south of the peninsula have identified multiple reverse faults that have been recently activated and that could be responsible for the rejuvenated uplift (Bruns et al., 2002; Ryan et al., 2008). These studies show a complex interaction of fault strands that creates localized areas of extension and contraction that have migrated in time and space as strike-slip motion continues on this network of interacting faults. For example, the San Gregorio Fault, which has been shown to have a late Pleistocene slip rate of 3.4–4.5 m/ka (Simpson and Lettis, 1999), merges with the SAF just south of Bolinas at what appears to be a restraining bend producing contraction west of the SAF, whereas the Golden Gate Fault appears to step left to the SAF producing a small extensional area east of the SAF (Fig. 1).

Measurements along the northern transect (WVT; Fig. 2) suggest that uplift rates were decreasing during the past several hundred thousand years, while uplift was increasing to the south. The orientation of the coastline is oblique to the structural trend, with the northernmost transect located closer to the hinge of the large-scale syncline (Fig. 2) and the southern transects located farther from the fold hinge and closer to the faults that have caused uplift of the eastern fold limb. The decreasing uplift rate at WVT is probably related to down-flexing near the hinge during development of the synclinal structure—a signal of ongoing deformation during the time that movement on faults to the south was causing accelerated uplift there.

The ages and correlations of uplifted marine terraces on other parts of the peninsula are uncertain. North of the WVT transect the upper terrace levels could be correlated along Inverness Ridge, but the lower levels could not, because north of WVT the lower terraces were formed by fluvial incision and aggradation, as the western limb (Point Reyes headland) was beginning to be uplifted and blocking the eastern ridge from direct wave attack, and so their timing does not directly correlate with the lower terraces on the WVT–BOL transects that were formed as wave-cut platforms. The terrace flights terminate at the north end of Inverness Ridge at a steep slope that was probably a sea cliff throughout the early stages of ridge uplift. North of Inverness Ridge is a low-lying bowl-shaped area extending to the south end of Tomales Point (Fig. 2) that would have been a shallow part of the ocean during those early uplift stages. East–west-trending faults at Kehoe Beach (Fig. 2) appear to have more recently uplifted Tomales Point, which has a terrace flight with 4–5 levels. No dateable sediments were found on the platform surfaces and so the timing of their uplift is uncertain.

On the west side of the PRP, the western limb of the Point Reyes syncline is probably being uplifted by motion on the Point Reyes thrust fault (Fig. 2), which has been identified on high-resolution and deep-penetration seismic lines west and south of the Point Reyes headland (McCulloch, 1989; Grove and Ryan, 2007). The uplift rate of this western limb is uncertain because of uncertainty about the origin of the sampled terrace sediments and the terrace age. If the sediment is marine sand deposited on a bedrock platform (103-m elevation) that was cut during the MIS 5a sea-level high stand (~80 ka), then the uplift rate would be ~1.3 m/ka. Because there is only one terrace on the western limb, which has a much lower overall elevation than the eastern limb, it is certain that the western limb has been uplifted

above sea level much more recently than the eastern limb, where ~11 terrace levels are observed.

Additional offshore investigations are needed to confirm the movement history of the offshore faults. But onshore observations can be made along the eastern side of the Inverness Ridge, where the WBF (Fig. 2) forms the eastern boundary of the uplifted block. Initial observations of landforms, using the Spatial Analyst extension in ArcGIS, showed that facets along the eastern flank of Inverness Ridge are higher and steeper to the south. We therefore conducted a geomorphic analysis to see if these results were consistent with our observations of differential uplift rates on the peninsula.

4. Geomorphic analyses

Quantitative measures of geomorphic attributes are commonly used to infer spatial variations in crustal uplift rates and the erosional response of landscapes to shifts in tectonic or climatic forcing (Burbank and Anderson, 2001; Hovius et al., 2004). Here we used spatial distributions of hillslope gradient and elevation, for a suite of watersheds draining the eastern flank of Inverness Ridge, to test whether the pattern of crustal uplift indicated by the terrace ages is expressed in the topography of the ridge (Table 4). In particular, we looked for geomorphic evidence that crustal uplift rates increase from north to south along the ridge, and that the accelerating crustal uplift to the south has produced active surface uplift and disequilibrium between rates of erosion and crustal uplift.

We analyzed 15 watersheds along the eastern flank of the Point Reyes Peninsula (Fig. 1), where vertical uplift of Inverness Ridge has presumably produced relative base-level fall at the downstream outlet of these small drainage networks where they flow into the SAF valley. We selected only watersheds that extend to the ridge crest and that are within or close to the range of locations along the trend of the ridge where dated terraces occur on the western side. This set of watersheds has the advantage of having relatively similar drainage basin sizes and shapes, without any significant variation in precipitation patterns. There is, however, a shift in bedrock type, with the northern watersheds (1e–6e) eroding into granodiorite, and the southern watersheds (7e–15e) eroding into marine sedimentary rocks of the Miocene Monterey Formation and Santa Cruz Mudstone. The granodiorite is deeply weathered, and the Monterey/Santa Cruz units consist of relatively resistant rock types (chert and siliceous mudstone), so the difference in competency among these rock types is not large. In any case, the observed changes described below occur within the sedimentary units.

We also analyzed watersheds on the western flank of Inverness Ridge, but determined that they are not useful for meaningful

comparisons for several reasons. First, the western watersheds have highly variable shapes and sizes, which can strongly affect watershed hypsometry (Willgoose and Hancock, 1998; Hurtrez et al., 1999). Second, much of the western flank is drained by a few large watersheds within which we would expect spatially variable uplift and erosion rates, confounding the slope distribution signal. Finally, it was difficult to determine the effective watershed outlet point, where uplift-driven relative base-level fall could be inferred, because of the north to south emergence over time of the eastern limb of the Point Reyes syncline. Complete results of all analyses can be found in Lee (2008).

Each watershed was delineated by generating stream networks from the 10-m DEM, using pour points located just upstream of where streams enter the broad valley created by the main strand of the SAF. We extracted hillslope gradients for each pixel, classified into 2.5°-wide bins, and calculated the mean and 95th percentile slope for each watershed. To analyze watershed hypsometry (the areal distribution of elevation), we used a custom Python ArcGIS geoprocessing script to extract planimetric surface area in elevation increments of 10 m. We assigned a location along the trend of Inverness Ridge to each watershed by projecting a line normal to the trend from the center of each watershed (Fig. 1).

To compare watershed geomorphic attributes with estimates of local crustal uplift rate estimates, derived from terrace analysis, we projected terrace transect locations onto the trend of Inverness Ridge and fit a curve to the uplift data from the youngest (80 ka) terrace ages (Fig. 6). We used an exponential function because it agrees well with the data ($R^2 = 0.93$; $p < 0.002$) and because it predicts positive uplift rates for the northern watershed locations, consistent with the broad tectonic interpretation presented above.

Hillslope gradients correlate with rates of down-slope sediment transport in soil-mantled landscapes (Carson and Kirkby, 1972; McKean et al., 1993) and with long-term average rates of landscape denudation (Granger et al., 1996; Binnie et al., 2007). Denudation rates measured, for example, with cosmogenic radionuclide (CRN) concentrations in stream sediments, are often used as proxies for rates of crustal uplift. This is done with the assumption that the response time of topographic adjustments is rapid compared to the rate of change of uplift rate, so that, over the time scale of CRN sample ages, the average erosion rate equals the rate of relative base-level lowering (e.g., Montgomery, 2001). Denudation rates have been shown to increase linearly with hillslope gradient at relatively low slopes (mean slope angle of $< 30^\circ$), and to increase non-linearly as slopes steepen toward a limiting, maximum stable slope angle. At this threshold slope, the denudation rate is controlled by the frequency of landsliding rather than by topographic gradients (Burbank et al., 1996; Hovius et al., 1997).

Table 4

Data for watersheds on eastern flank of Inverness Ridge.

Watershed ^a	Uplift rate (m/ka) ^b	Mean slope (degrees)	95th % slope (degrees)	Hypsometric integral
1e	0.11	20.4	34.4	0.400
2e	0.12	20.5	34.6	0.441
3e	0.13	21.8	35.6	0.443
4e	0.16	21.2	34.8	0.541
5e	0.19	18.7	33.1	0.453
6e	0.22	22.8	38.0	0.495
7e	0.25	22.0	37.7	0.417
8e	0.34	20.6	38.3	0.538
9e	0.37	22.8	39.2	0.573
10e	0.40	22.6	37.1	0.496
11e	0.43	26.3	40.2	0.498
12e	0.49	23.7	38.0	0.574
12e	0.53	23.4	38.4	0.570
14e	0.55	26.8	40.5	0.550
15e	0.60	22.5	36.8	0.554

^a Watersheds on Fig. 1; 1e = northwest end; 15e = southeast end.

^b Predicted crustal uplift rates from Fig. 6.

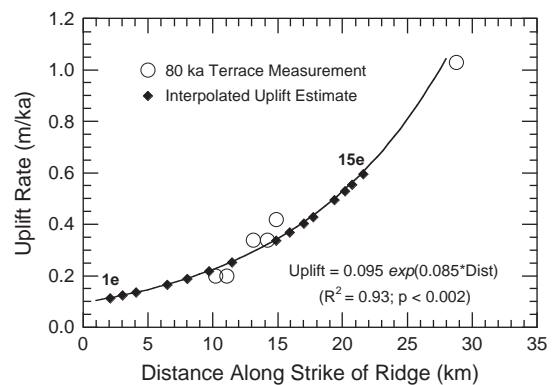


Fig. 6. Curve fit to measured crustal uplift rates for youngest terrace along each transect (open circles) and predicted crustal uplift rates for eastern watersheds (filled triangles), as a function of position along the trend of Inverness Ridge (distance increases to the south).

The spatial variation in hillslope gradients in the watersheds draining the eastern flank of Inverness Ridge is consistent with the crustal uplift gradient inferred from the terrace analysis. Fig. 7A shows the cumulative distributions of hillslope gradients for the 15 watersheds. Most slopes lie in the moderate range between 10 and 30°, although slopes above 40° occur for a small fraction of the landscape. As shown in Fig. 7B, mean watershed slopes generally steepen with increasing crustal uplift rate, with the lowest mean slopes occurring in the northern part of the study area and the steepest mean slopes in the south. A linear fit to the data is significant at the 99.6% level and explains about half of the variability. Also shown in Fig. 7B are the 95th percentile slopes for each watershed slope distribution, which appear to increase with crustal uplift rate but reach a constant average value of ~39° for uplift rates >0.3 m/ka. This result suggests that threshold slopes occur along the southern portion of the ridge, and is consistent with the observation that landslides are more common to the south. The change occurs within marine sedimentary rocks, not between granodiorite and sedimentary rocks, consistent with a tectonic rather than a rock-type control.

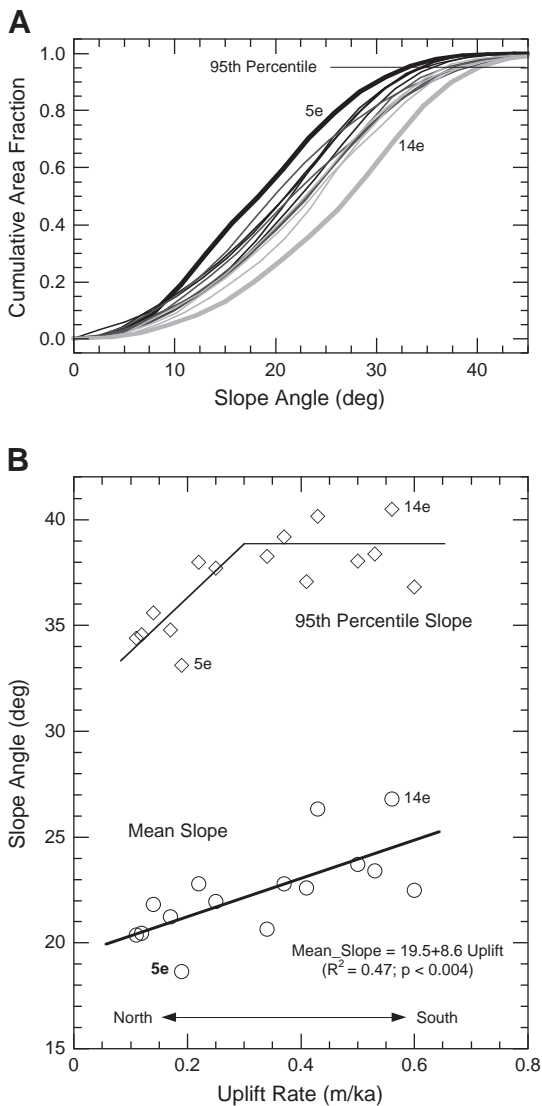


Fig. 7. A) Distributions of hillslope angles for 15 watersheds on east flank of Inverness ridge; watersheds 5e and 14e have least steep and most steep slopes, respectively. B) Mean and 95th percentile slope angles versus predicted crustal uplift rate showing increasingly steep hillslopes as uplift rate increases to the south; regression line fit to mean slope data, but for 95th percentile, line was fit-by-eye to illustrate apparent plateau as threshold slopes occur at higher uplift rates.

The hypsometric curve—the frequency distribution of elevation within a watershed—is a measure of the degree of landscape dissection, and can be compared across watersheds to infer transient response to changes in rates of tectonic forcing (Strahler, 1952), or spatial variation in the dominant erosional process (Montgomery et al., 2001). The curve describes the fraction of the total drainage area that lies below a given elevation, where the elevation is normalized by the maximum elevation in the watershed. The hypsometric integral is the area under the curve, and is constrained to be between 0 and 1. Typical values for fluvial landscapes, such as Inverness Ridge, range between 0.3 and 0.6 (Brocklehurst and Whipple, 2004). High values of the hypsometric integral occur in landscapes that are less dissected, where a greater fraction of the drainage area lies at relatively high elevations. This could occur during transient landscape evolution, where crustal uplift rates are more rapid than erosion rates (i.e., active surface uplift), and signal that accelerated relative base-level lowering rate has not yet propagated fully through the fluvial system. In fluvial landscapes, if denudation rates are approximately equal to crustal uplift rates (i.e., no active surface uplift), higher values of the hypsometric integral might reflect a greater role of landsliding versus creep in hillslope erosion, as would occur with more rapid rates of crustal uplift.

The hypsometric curves of the 15 watersheds along Inverness Ridge change systematically with estimated crustal uplift rate, with the topography becoming increasingly dissected as crustal uplift rates decline toward the north. As shown in Fig. 8A, the hypsometric curves plot highest and most convex toward the southern end of the ridge (toward watershed 15e), and become increasingly concave toward the north (toward watershed 1e). The hypsometric integrals range between 0.4 and 0.6, with a strong positive correlation with crustal

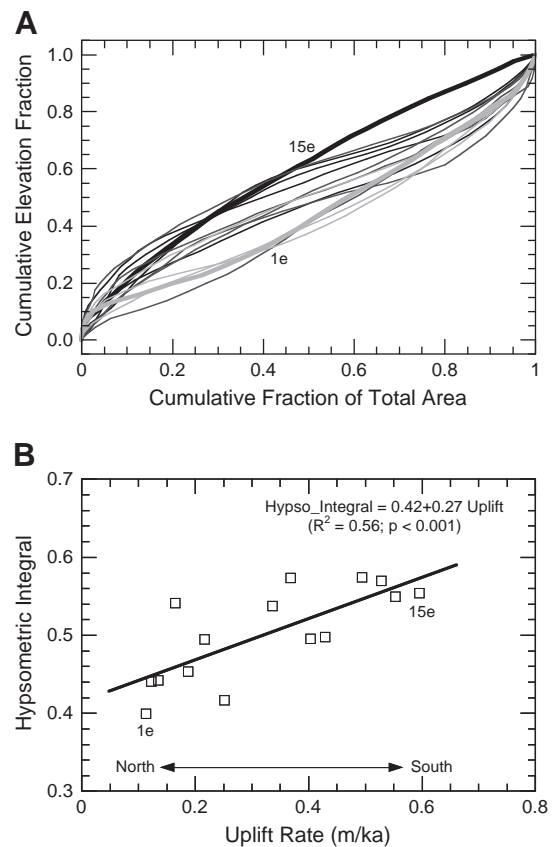


Fig. 8. A) Hypsometric curves for 15 eastern watersheds. B) Variation in hypsometric integral with predicted crustal uplift rate along Inverness Ridge, showing greater fraction of watershed area at higher relative elevations with increasing crustal uplift rate.

uplift rate (Fig. 8B). A linear fit to the data is significant at the 99.9% level and explains more than half of the variability. Hypsometric integrals increase within similar rock types, with no abrupt changes at rock type boundaries, and are therefore not controlled by bedrock type. We interpret the gradient in hypsometric integral as consistent with the tectonic model suggested by the terrace data, showing an increase in both crustal uplift rates and the rate of change in crustal uplift toward the southern end of the Inverness Ridge.

5. Discussion

Our study, the first to analyze uplift on the Point Reyes Peninsula (PRP), integrates two independent data sets—measured elevations of marine terrace flights and spatial distributions of two geomorphic attributes (hill slope gradient and elevation). These data sets have produced a consistent story of increasing uplift rates toward the south along Inverness Ridge. Deformation of the youngest terrace indicates that this differential uplift has continued during the past 80 ka, and modeling of terrace flight elevations suggests that the rate of uplift has accelerated during the past several hundred thousand years. As the first study to document recent and rapid uplift, we need to explore the potential reasons for the observations.

In the strike–slip-dominated tectonic environment on the coast of California, marine terraces along the western flank of the Santa Cruz Mountains, south of San Francisco and the study area, have high uplift rates (up to 1 m/ka; Anderson and Menking, 1994; Perg et al., 2001) because of a bend in the SAF that is oriented ~15° counterclockwise to the direction of Pacific Plate–Sierra microplate motion (Argus and Gordon, 2001). To the north of the study area, near Point Arena, the counterclockwise orientation of the SAF relative to plate motion predicts uplift rates similar to those found in the Santa Cruz Mountains (Argus and Gordon, 2001). Indeed, a rate of ~0.5 m/ka has been calculated at Point Arena, based on U-series dating of coral on the youngest (~80 ka terrace; Muhs et al., 1990), and the highest measured uplift rates (~4 m/ka) in northern California are found near the Mendocino triple junction where lithospheric interactions are complex and heat flow is high (Merritts and Bull, 1989; Furlong, 1993). At the latitude of Point Reyes, the SAF is nearly parallel to the plate motion direction (Argus and Gordon, 2001) and reverse faulting is likely to be the result of complex fault interactions and restraining bend/step-over geometries. On their transect, which extends across the southern part of the PRP and northern San Francisco Bay, Argus and Gordon (2001) found negative convergence plate rates (-2.6 ± 1.2 m/ka), implying a significant net divergence. This extension may be expressed in the low-lying San Pablo Bay (Fig. 1), and the convergence we have observed in the southern part of the PRP is probably a result of the fault interactions that occur in the offshore zone south and west of the peninsula (Bruns et al., 2002; Ryan et al., 2008).

The offshore zone south of the PRP is distinctively complex in terms of its rapid spatial and temporal variations. Currently, a right step or bend in the SAF (Zoback et al., 1999) is producing a Holocene graben between the SAF and the Golden Gate Fault just south of Bolinas lagoon (Bruns et al., 2002; Fig. 1). Over a narrow zone of ~2 km, deformation changes westward from extension in the graben to contraction in a series of folds and reverse faults off the southwest coast of Bolinas (Ryan et al., 2008; San Gregorio structural zone of Bruns et al., 2002). The contractional zone consists of faults that extend to the seafloor and that appear to have been recently reactivated (Bruns et al., 2002; Grove and Ryan, 2007). The Point Reyes thrust fault, which curves around the south end of the Point Reyes headland and is probably responsible for its uplift, may connect farther south with the western strand of the San Gregorio Fault (SGF-W on Fig. 1) that forms the western edge of the contractional zone (McCulloch, 1989; Ryan et al., 2008). The 1999 ~M5 earthquake near Bolinas (Fig. 2) occurred on a 45°-dipping reverse fault that projects upward to a position near the Point Reyes/San Gregorio-west

fault and implies that this fault may be active and responsible for at least some of the uplift observed on the PRP. Movement on a complex array of strike–slip faults with varying strikes in the offshore zone between the Point Reyes and San Francisco Peninsulas (Fig. 1) has led to intricate geometries that create areas of extension and contraction within extremely short distances. Continued movement along these strands rearranges the fault geometries, and blocks between faults alternatively subside or are uplifted as they migrate through releasing or constraining geometries. Although uplift rates were relatively slow throughout most of the period during which the PRP was being uplifted, it appears that rates have recently accelerated at the south end of the peninsula because a contractional zone has been migrating northward.

At a dextral slip rate of 24 ± 3 m/ka (Niemi and Hall, 1992), the PRP at 1 Ma would have been located about 24 km farther south and directly west of the Golden Gate. At that time most of the peninsula was probably below sea level, at least at high-stand levels, and Inverness Ridge would have been an emerging island. A combination of fluctuating sea levels and island uplift created the flight of terraces that are visible today. By 300 ka, uplift in the southern part of the island/peninsula was accelerating; by 100 ka, uplift rates had reached nearly 1.0 m/ka, and the headland at Point Reyes was being uplifted above (present-day) sea level. As uplift has continued, more parts of the peninsula have been removed from wave attack, although fluvial processes have continued to create terrace surfaces in those areas.

6. Conclusions

Elevations of marine terraces along the western coast of the PRP show that crustal uplift rates are higher toward the southern end, reaching ~1 m/ka near Bolinas. Quantitative measurements of geomorphic attributes are consistent with the observation of southward-increasing rates. Although the PRP appears to have been uplifting slowly during most of the past 1–2 Ma, during the past ~300 ky uplift of the southern end appears to have accelerated, as a contractional zone in the offshore region south of the peninsula has migrated northward. Other than a ~M5 earthquake caused by movement on a reverse fault west of Bolinas, this study is the first documented evidence of contractional deformation associated with this part of the San Andreas Fault. Results imply that reverse faults in the region have been active during the past 80 ky, and that their earthquake potential should be investigated.

Acknowledgements

We wish to thank the Point Reyes National Seashore for granting permission to collect data within the park. Research was partially funded by Petroleum Research Fund Grant #35199-B2 (administered by American Chemical Society). We thank San Francisco State students who contributed undergraduate research—T. Bidgoli, J. Davis, L. Harliss, A. Laubhan, L. Pawlak—or helped with field work—A. Biggar, R. Ford, B. Fuller, J. Goodman, J. Hamm, and B. Sas. We thank D. Merritts and C. Prentice for sharing results and methods from their Keck Research Opportunities for Undergraduates project. Conversations with John Caskey, and thorough reviews by Dan Muhs and Rob Westaway, helped to improve the manuscript.

References

- Aitken, M.J., 1998. An Introduction to Optical Dating. Oxford University Press, 267 pp.
- Anderson, R.S., Menking, K.M., 1994. The Quaternary marine terraces of Santa Cruz, California: evidence for coseismic uplift on two faults. *Geological Society of America Bulletin* 106, 649–664.
- Argus, D.F., Gordon, R.G., 2001. Present tectonic motion across the Coast Ranges and San Andreas Fault system in central California. *Geological Society of America Bulletin* 113, 1580–1592.
- Binnie, S.A., Phillips, W.M., Summerfield, M.A., Fifield, L.K., 2007. Tectonic uplift, threshold hillslopes, and denudation rates in a developing mountain range. *Geology* 35, 743–746.
- Bradley, W.C., Griggs, G.B., 1976. Form, genesis, and deformation of central California wave-cut platforms. *Geological Society of America Bulletin* 87, 433–449.

- Brocklehurst, S.H., Whipple, K.X., 2004. Hypsometry of glaciated landscapes. *Earth Surface Processes and Landforms* 29, 907–926.
- Bruns, T.R., Cooper, A.K., Carlson, P.R., McCulloch, D.S., 2002. Structure of the submerged San Andreas and San Gregorio fault zones in the Gulf of the Farallones off San Francisco, California, from high-resolution seismic-reflection data. In: Parsons, T. (Ed.), *Crustal Structure of the Coastal and Marine San Francisco Bay Region, California*: U.S. Geological Survey Professional Paper, 1658, pp. 77–117.
- Burbank, D.W., Anderson, R.S., 2001. *Tectonic Geomorphology*. Malden, Blackwell Science, Inc., 275 pp.
- Burbank, D.W., Leland, J., Fielding, E., Anderson, R.S., Brozovic, N., Reid, M.R., Duncan, C., 1996. Bedrock incision, rock uplift and threshold hillslopes in the Northwestern Himalayas. *Nature* 379, 505–510.
- Carson, M.A., Kirkby, M.J., 1972. *Hillslope Form and Process*. Cambridge University Press, London, 475 pp.
- Chappell, J.M., Shackleton, N., 1986. Oxygen isotopes and sea level. *Nature* 324, 137–140.
- Chappell, J., Omura, A., Esat, T., McCulloch, M., Pandolfi, J., Ota, Y., Billans, B., 1996. Reconciliation of late Quaternary sea levels derived from coral terraces at Huon Peninsula with deep sea oxygen isotope records. *Earth and Planetary Science Letters* 141, 227–236.
- Claessens, L., Veldkamp, A., ten Broeke, E.M., Vloemans, H., 2009. A Quaternary uplift record for the Auckland region, North Island, New Zealand, based on marine and fluvial terraces. *Global and Planetary Change* 68, 383–394.
- Clague, J.J., 1969. Landslides of southern Point Reyes National Seashore. *Mineral Information Service* 22 (7), 107–118.
- Clark, J., Brabb, E., 1997. *Geology of Point Reyes National Seashore and Vicinity, California: A Digital Database*. U.S. Geological Survey Open-File Report 97–456.
- Clark, J.C., Brabb, E., Greene, H.G., Ross, D.C., 1984. *Geology of Point Reyes Peninsula and implications for San Gregorio fault history*. In: Crouch, J.K., Bachman, S.B. (Eds.), *Tectonics and Sedimentation along the California Margin*: SEPM Pacific Section, 38, pp. 67–85.
- D'Alessio, M.A., Johanson, I.A., Burgmann, R., 2005. Slicing up the San Francisco Bay area: block kinematics and fault slip rates from GPS-derived surface velocities. *Journal of Geophysical Research* 110 (B06403). doi:10.1029/2004JB003496.
- Duller, G.A.T., 2004. Luminescence dating of Quaternary sediments: recent advances. *Journal of Quaternary Science* 19, 183–192.
- Furlong, K.P., 1993. Thermal-rheologic evolution of the upper mantle and the development of the San Andreas Fault system. *Tectonophysics* 223, 149–164.
- Galloway, A.J., 1977. *Geology of the Point Reyes Peninsula, Marin County, California*. California Division of Mines and Geology Bulletin, 202, 72 pp.
- Granger, D.E., Kirchner, J.W., Finkel, R., 1996. Spatially averaged long-term erosion rates measured from in-situ-produced cosmogenic nuclides in alluvial sediment. *Journal of Geology* 104, 249–257.
- Grove, K., Niemi, T., 2005. Late Quaternary deformation and slip rates in the northern San Andreas fault zone at Olema Valley, Marin County, California. *Tectonophysics* 401, 231–250. doi:10.1016/j.tecto.2005.03.014.
- Grove, K., Ryan, H., 2007. Marine terrace and offshore seismic evidence for spatially and temporally varying uplift rates adjacent to the San Andreas Fault north of San Francisco, California. *Geological Society of America Abstracts with Programs* 39 (6), 239.
- Hall, N.T., Wright, R.H., Clahan, K.B., 1999. Paleoseismic studies of the San Francisco Peninsula segment of the San Andreas fault zone near Woodside, California. *Journal of Geophysical Research* 104, 23215–23236.
- Hoskins, E.G., Griffiths, J.R., 1971. Hydrocarbon potential of northern and central California offshore. *American Association of Petroleum Geologists Memoir* 15, 212–228.
- Hovius, N., Stark, C.P., Allen, P.A., 1997. Sediment flux from a mountain belt derived by landslide mapping. *Geology* 25, 231–234.
- Hovius, N., Lague, D., Dadson, S., 2004. Processes, rates and patterns of mountain-belt erosion. In: Owens, P.N., Slaymaker, O. (Eds.), *Mountain Geomorphology*. Oxford University Press, pp. 109–131.
- Hurtrez, J.E., Sol, C., Lucazeau, F., 1999. Effect of drainage area on hypsometry from an analysis of small-scale drainage basins in the Siwalik Hills (central Nepal). *Earth Surface Processes and Landforms* 24, 799–808.
- Jachens, R.C., Wentworth, C.M., Zoback, M.L., Bruns, T.R., Roberts, C.W., 2002. Concealed strands of the San Andreas Fault system in the central San Francisco Bay Region, as inferred from aeromagnetic anomalies. In: Parsons, T. (Ed.), *Crustal Structure of the Coastal and Marine San Francisco Bay Region, California*: U.S. Geological Survey Professional Paper, 1658, pp. 43–61.
- Johnson, C.B., Furlong, K.P., Kirby, E., 2009. Integrated geomorphic and geodynamic modeling of a potential blind thrust in the San Francisco Bay area, California. *Tectonophysics* 471, 319–328. doi:10.1016/j.tecto.2009.03.002.
- Kirby, E., Johnson, C., Furlong, K., Heimsath, A., 2007. Transient channel incision along Bolinas Ridge, California: evidence for differential rock uplift adjacent to the San Andreas Fault. *Journal of Geophysical Research* 112 (F03S07). doi:10.1029/2006JF000559.
- Lajoie, K.R., 1986. Coastal tectonics. In: Usselman, T.M. (Ed.), *Active Tectonics*. Washington D.C., National Academy Press, pp. 95–124.
- Lawson, A.C., 1908. *The California Earthquake of April 18, 1906*, Report of the State Earthquake Investigation Commission. chairman Publication 87, Carnegie Institution, Washington, D.C. [reprinted 1969].
- Lee, G., 2008. *Geomorphic expression of differential uplift, Point Reyes Peninsula, Marin County, California* [Master's thesis]. San Francisco State University, 109 pp.
- Lian, O.B., Roberts, R.G., 2006. Dating the Quaternary: progress in luminescence dating of sediments. *Quaternary Science Reviews* 25, 2449–2468.
- Lisiecki, L.E., Raymo, M.E., 2005. A Pliocene–Pleistocene stack of 57 globally distributed benthic $\delta^{18}\text{O}$ records. *Paleoceanography* 20. doi:10.1029/2004PA001071 PA 1003.
- Litchfield, N.J., Lian, O.B., 2004. Luminescence age estimates of Pleistocene marine terrace and alluvial fan sediments associated with tectonic activity along coastal Otago, New Zealand. *New Zealand Journal of Geology and Geophysics* 47, 29–37.
- McCulloch, D.S., 1989. Evolution of an offshore central California margin. In: Winterer, E.L., Hussong, D.M., Drecker, R.W. (Eds.), *The Eastern Pacific Ocean and Hawaii*. Boulder, Colorado, Geological Society of America, The Geology of North America, V. N, pp. 439–456.
- McInelly, G.W., Kelsey, H.M., 1990. Late Quaternary tectonic deformation in the Cape Arago–Brandon region of coastal Oregon as deduced from wave-cut platforms. *Journal of Geophysical Research* 95, 6699–6713.
- McKean, J.A., Dietrich, W.E., Finkel, R.C., Southon, J.R., Caffee, M.W., 1993. Quantification of soil production and downslope creep rates from cosmogenic ^{10}Be accumulations on a hillslope profile. *Geology* 21, 343–346.
- Merritts, D., Bull, W.B., 1989. Interpreting Quaternary uplift rates at the Mendocino triple junction, Northern California, from uplifted marine terraces. *Geology* 17, 1020–1024.
- Millard Jr., H.T., Maat, P.B., 1994. Thermoluminescence dating procedures in use at the U.S. Geological Survey, Denver, Colorado. U.S. Geological Survey Open-File Report 94-249, 112 pp.
- Montgomery, D.R., 2001. Slope distributions, threshold hillslopes, and steady state topography. *American Journal of Science* 301, 432–454.
- Montgomery, D.R., Balco, G., Willet, S.D., 2001. Climate, tectonics, and the morphology of the Andes. *Geology* 29, 579–582.
- Muhs, D.R., 2000. Dating marine terraces with relative-age and correlated-age methods. In: Noller, J.S., Sowers, J.M., Lettis, W.R. (Eds.), *Quaternary Geochronology: Methods and Applications*: American Geophysical Union, Reference Shelf, 4, pp. 434–446.
- Muhs, D.R., Kelsey, H.M., Miller, G.H., Kennedy, G.L., Whelan, J.F., McInelly, G.W., 1990. Age estimates and uplift rates for late Pleistocene marine terraces: southern Oregon portion of the Cascadia forearc. *Journal of Geophysical Research* 95 (B5).
- Muhs, D.R., Kennedy, G.L., Rockwell, T.K., 1994. Uranium-series ages of marine terrace corals from the Pacific coast of North America and implications for the last-interglacial sea level history. *Quaternary Research* 42, 72–87.
- Muhs, D.R., Simmons, K.R., Kennedy, G.L., Rockwell, T.K., 2002. The last interglacial period on the Pacific coast of North America: timing and paleoclimate. *Geological Society of America Bulletin* 114, 569–592.
- Muhs, D.R., Prentice, C., Merritts, D.J., 2003a. Marine terraces, sea level history and Quaternary tectonics of the San Andreas Fault on the coast of California. In: Easterbrook, D. (Ed.), *Quaternary Geology of the United States*. INQUA 2003 Field Guide Volume, Desert Research Institute, Reno, NV, pp. 1–18.
- Muhs, D.R., Wehmiller, J.F., Simmons, K.R., York, L.L., 2003b. Quaternary sea-level history of the United States. In: Gillespie, A.R., Porter, S.C., Atwater, B.F. (Eds.), *The Quaternary Period in the United States*, vol. 1. Elsevier, pp. 147–183. doi:10.1016/S1571-0866(03)01008-X.
- Murray, A.S., Funder, S., 2003. Optically stimulated luminescence dating of a Danish Eemian coastal marine deposit: a test of accuracy. *Quaternary Science Reviews* 22, 1177–1183.
- NCEDC (Northern California Earthquake Data Center), cited 2004. <http://quake.geo.berkeley.edu/ncedc/catalog-search.html>.
- Niemi, T.M., Hall, N.T., 1992. Late Holocene slip rate and recurrence of great earthquakes on the San Andreas Fault in northern California. *Geology* 20, 195–198.
- Perg, L.A., Anderson, R.S., Finkel, R.C., 2001. Use of a new ^{10}Be and ^{26}Al inventory method to date marine terraces, Santa Cruz, California, USA. *Geology* 29, 879–882.
- Prescott, J.R., Robertson, G.B., 2008. Luminescence dating: an Australian perspective. *Australian Journal of Earth Sciences* 55, 997–1007.
- Richardson, C.A., 2001. Residual luminescence signals in modern coastal sediments. *Quaternary Science Reviews* 20, 887–892.
- Rostami, K., Peltier, W.R., Mangini, A., 2000. Quaternary marine terraces, sea-level changes and uplift history of Patagonia, Argentina: comparisons with predictions of the ICE-4 G (VM2) model of the global process of glacial isostatic adjustment. *Quaternary Science Reviews* 19, 1495–1525.
- Ryan, H.F., Parsons, T., Sliter, R.W., 2008. Vertical tectonic deformation associated with the San Andreas Fault offshore of San Francisco, California. *Tectonophysics* 475, 209–223. doi:10.1016/j.tecto.2008.06.011.
- Rypins, S., Reneau, S.L., Byrne, R., Montgomery, D.R., 1989. Palynologic and geomorphic evidence for environmental change during the Pleistocene–Holocene transition at Point Reyes Peninsula, central coastal California. *Quaternary Research* 32, 72–87.
- Santorio, E., Mazzella, M.E., Ferranti, L., Randisi, A., Napolitano, E., Rittner, S., Radtke, U., 2009. Raised coastal terraces along the Ionian Sea coast of northern Calabria, Italy, suggest space and time variability of tectonic uplift rates. *Quaternary International* 206, 78–101.
- Scherer, A.M., 2004. *Geographic information system analyses of Quaternary marine terraces, Point Reyes Peninsula, California* [Master's thesis]. San Francisco State University, 122 pp.
- SEP (Special Earthquake Report) No: 99–018, cited 1999. <http://www.seismowatch.com/EQS/AB/99/990817.Bolinas5.0.html>.
- Simpson, G.D., Lettis, W.R., 1999. Slip rate and earthquake history of the northern San Gregorio Fault, Half Moon Bay to Moss Beach, California. *American Association of Petroleum Geologists Bulletin* 83 (4), 701.
- Strahler, A.N., 1952. Hypsometric (area-altitude) analysis of erosional topography. *Geological Society of America Bulletin* 63, 1117–1141.
- Wakabayashi, J., 1999. Distribution of displacement on and evolution of a young transform fault system: the northern San Andreas fault system, California. *Tectonics* 18, 1245–1274.
- Willgoose, G., Hancock, G., 1998. Revisiting the hypsometric curve as an indicator of form and process in transport-limited catchment. *Earth Surface Processes and Landforms* 23, 611–623.
- Zoback, M.L., Jachens, R.C., Olson, J.A., 1999. Abrupt along-strike change in tectonic style: San Andreas Fault zone, San Francisco Peninsula. *Journal of Geophysical Research* 104 (B5), 10719–10742.